Journal of Materials Chemistry A

Accepted Manuscript

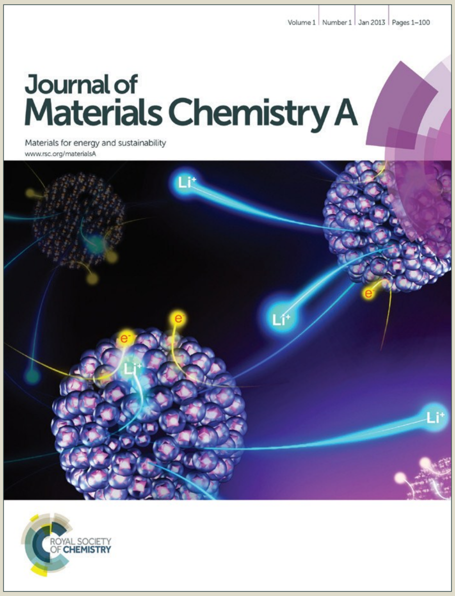

ROYAL SOCIETY OF CHEMISTRY

www.rsc.org/materialsA

Hydrothermal Growth of Few Layer 2H-MoS_2 for Heterojunction Photodetector and Visible Light Induced Photocatalytic Applications

*Anupam Midya,[1] Arup Ghorai,[1] Subhrajit Mukherjee,[2] Rishi Maiti,[3] Samit K Ray[1,3]**

[1]*School of Nanoscience and Technology, Indian Institute of Technology Kharagpur, Kharagpur 721302*
[2]*Advanced Technology Development Centre, Indian Institute of Technology Kharagpur, Kharagpur 721302*
[3]*Department of Physics, Indian Institute of Technology Kharagpur, Kharagpur 721302*
**Email: physkr@phy.iitkgp.ernet.in*

Abstract

The present low yield growth techniques of semiconducting 2H phase molybdenum disulfide (MoS_2) hamper its widespread applications. In this article, we report a novel hydrothermal chemical approach to synthesize micron sized few layer 2H MoS_2 in large scale. Sodium molybdate and ammonium thiocyanate have been used as precursors to obtain template free 2H MoS_2 in solution. Detailed microscopic and spectroscopic characterizations reveal that the bottom-up synthesized few layers MoS_2 flakes are highly crystalline having hexagonal 2H phase. Photodetector devices comprising p-type silicon (p-Si)/n-MoS_2 heterostructure have been fabricated for the first time using solution processed 2H MoS_2 synthesized by bottom up approach. The heterojunction diode exhibits a high rectification ratio ($> 10^3$) with broad band photoresponse over the visible range. Because of the visible light photoresponse, as-synthesized MoS_2 along with reduced graphene oxide (MoS_2-RGO hybrids) have been utilized to study the potential of two dimensional (2D) heterostructure for visible light driven photocatalytic Rhodamine B dye degradation. The study demonstrates the potential of solution processed MoS_2 for integration with silicon and growth of 2D heterostructure for visible light induced multifunctional applications.

Keywords: 2H MoS_2, RGO, photodetector, 2D hybrids, Rhodamine B, Photocatalysis.

Introduction:

Beyond graphene, a new two dimensional (2D) material, molybdenum disulfide (MoS_2) with a direct band gap of 1.82 eV, has attracted immense interests for electronic and optoelectronics applications. In 2D MoS_2, with a tri-atomic thick regime (S-Mo-S), Mo atoms are sandwiched between two layers of S atoms forming semiconducting 2H (trigonal prismatic D3h) and metallic 1T (octahedral Oh) phases. With the thickness depended extraordinary properties, layered MoS_2 has shown great promise as anode materials in lithium ion batteries,[1-3] interface layer in bulk heterojunction solar cells,[4,5] electrode coating in dye sensitized solar cells,[6-8] biomolecule sensor,[9] gas sensors,[10,11] photodetectors,[12,13] memory devices,[14,15] catalyst for the hydrogen evolution[16,17] and photocatalyst for dye degradations.[18] However, low yield production of highly crystalline, semiconducting, thin layer MoS_2 hinders its widespread applications in multifunctional devices. Among the available synthesis approaches, the sonication assisted liquid phase exfoliation results mostly smaller nanocrystals (3-12 nm thick and ~300 nm lateral dimensions)[19] due to scissoring of the sheets in all directions. Mimicking graphene exfoliation by scotch tape method,[20] MoS_2 layers can be obtained,[21] although the yield is very low and required exhausting transferring process for device applications. Toxic and highly flammable butyl lithium[22] or corrosive hydrazine[23] have been used to synthesize monolayer MoS_2 of 1T phase[24] in high yield, but an additional step, like a thermal annealing[25] or solvothermal heating[26,27] under an inert atmosphere, is required to transfer the phase from 1T to 2H, making the method tedious. On the other hand, wet chemical bottom-up approaches can provide thin 2H MoS_2 nanocrystals, using various Mo and S precursors and templates at hydrothermal or refluxing conditions. In most cases, sodium molybdate (Na_2MoO_4),[28] molybdenum oxide (MoO_3)[29] or ammonium tetrathiomolybdate ($(NH_4)_2MoS_4$)[30] was used as Mo sources while cysteine,[31] thiourea,[32] or elemental sulfur[33] was employed as S sources. In a wet chemical route, single and multilayer

MoS_2 with oleylamine coating were obtained by decomposition of $(NH_4)_2MoS_4$ at 360 °C.[34] However, it is a great challenge to achieve large scale production of micron sized monolayer or few layer 2H-MoS_2 by control wet chemical method without any templates.

In this article, we report a novel and environment friendly synthesis route for few layer 2H MoS_2 in solution phase using one step hydrothermal method. Na_2MoO_4 and ammonium thiocyanate (NH_4SCN) have been used as Mo and S sources, respectively. The dual role of thiocyante anion, as a 'S' source and reductant, is established on the wet chemical investigations of the end product mixture. Gaseous by-products and counter cations present in the reaction mixture inhibit the growth along c-axis resulting in thinner MoS_2 sheets. As a proof of concept, Si-complementary metal oxide semiconductor (CMOS) compatible 2D heterojunction photodiode has been fabricated using solution processed semiconducting MoS_2 on p-Si. The rectification characteristics and photoresponse of the heterojunction in the visible wavelength region are presented. In addition, graphene oxide (GO) has been used as a template to synthesize MoS_2-reduced GO (RGO) hybrids to study the potential of 2D heterostructure in visible light induced photo-catalytic dye degradation towards remediation of waste water. The RGO not only acts as a template, but also as a stabilizer and 2D platforms to adsorb pollutant dye molecules. The formation of an intimate contact between RGO and MoS_2 in the 2D hybrid facilitates photoinduced charge separation resulting in superior photocatalytic activity under visible light illumination as compared to as-synthesized bare MoS_2.

Experimental:

Materials: All the chemicals and solvents, purchased from Sigma Aldrich and Merck, were used without further purification. Ultrapure deionized (DI) water was used a as solvent throughout the experiments.

Synthesis of few layer 2H MoS_2

In a typical procedure, 0.0125 mol of ammonium thiocyanate (NH_4SCN) (0.95 g), or potassium thiocyanate (KSCN) (1.22 g) or sodium thiocyanate (NaSCN) (1.01 g) and 0.005 mol (1.21 gm) of sodium molybdate (Na_2MoO_4) were mixed homogeneously in 30 ml of deionised water. The whole mixture was taken into a 50 ml Teflon chamber sealed into a stainless steel tank and incubated at 250 °C for 24 hr followed by cooling at room temperature on standing. The obtained dark black sediment was washed by centrifugation (5000 rpm, 10 minutes) for five times with deionised water to remove the residue of the by-products and reactants. The as-synthesized wet MoS_2 sediment was transferred into the organic solvent such as *N,N* dimethyl formamide (DMF), propylene carbonate (PC), isopropyl alcohol (IPA), *N*-methylpyrrolidine (NMP) by mild sonication for 2 minutes to obtain a dark greenish solution.

Synthesis of MoS_2-GO and MoS_2-RGO hybrid:

Following the above procedure, initially about 20 mg of graphene oxide (GO)[35] was added to the solution mixture of $NaMoO_6$ and potassium thiocyante before hydrothermal treatment. The MoS_2-GO hybrid was purified using sonication and centrifugation with DI water after hydrothermal treatment. The MoS_2-RGO hybrid in DI water was synthesized by incubating the solution with the exposure of a 200 W broadband (wavelength: 800–2000 nm) IR source for two different periods (2 and 6 hr) in an ambient condition and at a fixed distance of 5 cm (0.64 Wcm^{-2}). The dark greenish solution gradually turned black after being exposed to infrared (IR) light for 6 hr, indicating the occurrence of reduction. Chemical composition and purity of MoS_2-RGO hybrids were evaluated by X-ray photoelectron spectroscopy (XPS) and UV-visible spectroscopy, indicating the absence of any chemical change of MoS_2 other than the reduction of GO.

Heterojunction photodiode fabrication: A vertical p-Si/n-MoS_2 heterojunction diode was fabricated using simple solution processed MoS_2 layers. Briefly, 1 mg/ ml MoS_2 in iso-propanol solution was spin coated on top of the pre-cleaned p-Si (resistivity 7-14 ohm-cm) substrate at 800 rpm. The coated film was dried at 60 °C for 10 min. Finally top and bottom electrodes were deposited by sequentially evaporating Al metal at a chamber pressure of ~$1x10^{-6}$ Torr.

Photocatalysis: The photocatalytic performance of the MoS_2 and MoS_2-RGO hybrids under visible illumination was evaluated by monitoring the Rhodamine B (RhB), a pollutant organic dye, degradation reaction kinetics. The photochemical reactions were carried out in an aqueous solution under visible white light irradiation induced by a compact fluorescent lamp (28 W/cm^2). In a typical experimental procedure, 5 mg of catalysts was placed into 30 mL of 10^{-5} M RhB solution. To achieve adsorption equilibrium between the organic dye and catalysts, the reaction dispersion was kept stirring for 35 min in dark before visible light irradiation. 2 mL of the reaction mixture was pipetted out at an interval of 25 min and centrifuged at 1000 rpm to remove catalyst particles and the remaining concentration of RhB was determined by measuring the absorbance of RhB at 553 nm by UV-vis spectroscopy. Few control experiments were carried out to find out the reactive species involved for photocatalysis, in presence of triethanolamine (TEOA), tertiary butyl alcohol (t-BuOH) and in the absence of O_2 (under nitrogen environment.)

Characterizations: UV-visible absorption spectra of MoS_2 dispersion were recorded using a fiber-probe-based UV-Vis-NIR CCD spectrometer. The chemical composition of as-synthesized MoS_2 was evaluated using X-ray photoelectron spectroscopy (PHI 5000 Versa Probe II, ULVAC−PHI, INC, Japan) with an incident AlKα X-ray of energy hν = 1486.6 eV. Surface morphology and thickness of MoS_2 flakes were investigated using Veeco Nanoscope-III atomic force microscope (AFM). High resolution transmission electron microscope (HRTEM) (Model No JEM–2100) equipped with a charge couple device (CCD) camera from Gatan, Inc. USA, at an operating voltage 200 KV (JEOL, Japan) was used for bright-field imaging of MoS_2 layer structure. X-Ray diffraction (XRD) patterns of few layer MoS_2 and hybrids nanocomposites were recorded using a Philips MRD X-ray diffractometer (40 kV, 20 mA) with Cu Kα radiation ($\lambda = 1.5418$ Å) in the 2θ range of 5°–70° at a scanning rate of 0.5° min^{-1}.

Results and discussion

A critical control over crystal growth is mandatory to obtain 2D MoS_2 instead of bulk 3D MoS_2 in bottom up processing. In hydrothermal method, high pressure inside the autoclave chamber plays a crucial role on the formation of few layers MoS_2 instead of bulk MoS_2.[36] Here, some gaseous by-product or ions adsorbed on the surface of the layers inhibit the vertical growth of MoS_2, allowing only lateral growth, as shown schematically in the Figure 1. In the reaction process, thiocyante anion (SCN^-) plays dual role, as a reducing reagent as well as S source. To investigate the by-product of the reaction, we analyzed the resultant aqueous product mixture using aqueous barium chloride ($BaCl_2$) and calcium chloride ($CaCl_2$) solutions. Immediately, a large amount of white precipitation was obtained after adding $BaCl_2$. XRD pattern of the precipitate confirms it as barium sulphate ($BaSO_4$), which is insoluble in acid (Figure S1, electronic supplementary information (ESI)). Therefore Mo (VI) is reduced to Mo (IV) by some part of SCN^- which in turn is oxidized into SO_4^{2-}. The remaining portion of SCN^- forms MoS_2 with Mo (IV) as schematically shown in Figure 1. XRD pattern of calcium carbonate ($CaCO_3$) was obtained (Figure S2, ESI) on analyzing the precipitate appeared on treating the supernatant with Ca^{2+}. The presence of ammonia gas in the product mixture is confirmed by testing with Nessler's reagent. To get more information, we have performed the XRD measurements on the residue of supernatant without any detection of KCN, KOCN or NaCN. Thus, the possible reaction for the synthesis of MoS_2 could be formulated as

$$4MoO_4^{2-} + SCN^- + H_2O \longrightarrow MoS_2 + SO_4^{2-} + 3\,NH_4^+ + 9\,CO_3^{2-} + 6\,NH_3\,(g).$$

As-synthesized wet MoS_2 sediment has been re-dispersed only in polar solvents, such as dimethyl formamide, propylene carbonate, *N*-methylpyrrolidine and isopropyl alcohol etc., forming transparent greenish solutions (Figure S3, ESI)), which resemble to those derived from liquid phase exfoliated MoS_2.[37,38] Whereas, MoS_2-GO hybrid forms stable dark green aqueous solution, which is stable under visible light for months without any agglomeration (Figure S4, ESI). Simple photothermal reduction technique[39] has been used to synthesize MoS_2-RGO hybrids, avoiding purification, hazardous chemical interference on the photocatalyst performance.

Semiconducting nature of synthesized 2H MoS_2 nanosheets has been established by UV-vis absorption spectroscopy. Figure 2 (a) shows three distinct absorption peaks for MoS_2 in IPA solution at ~665 nm, ~618 nm and a broad one at ~450 nm. Two sharp peaks at 665 (1.86 eV) and 618 nm (2.0 eV) are the direct band gap transitions originated from the highest spin-splitted valence band edge due spin-orbital coupling to the lowest conduction band edge at the K-point of the first Brillouin zone.[40,41] The spin degeneracy at the valence-band edges arises purely from the combined effect of interlayer coupling and the spin–orbit interactions. A combination of time-reversal and translational symmetry results in zero splitting at the M point, whereas the spin splitting at K point is determined by time-reversal and D3h point-group symmetry.[40] At the K and K′ valleys in momentum space, the highest-energy valence bands and the lowest-energy conduction bands are mainly of molybdenum d-orbital character. The electronic band structure of MoS_2, consists of partially filled Mo d-orbitals between Mo and S, s-p bonding and antibonding bands. Therefore, the valence band reveals hybridization between the S p_z and Mo $d_3z^2{-}r^2$ states at that point (M-point). Towards the K point, these contributions are gradually replaced by the S $p_x + p_y$ and Mo $dx^2{-}y^2$ + dxy states. However, the conduction band-edge state is made of dz^2 orbitals and remains spin degenerate at K points. Approximating the spin-orbital coupling by the intra-atomic contribution of **L.S**, mainly the heavier transition-metal atoms (Mo) [$dx^2{-}y^2$ + dxy] states turn out to be responsible for the strong spin-orbit coupling leading to the giant spin splitting.[40,41] The broad peak at 450 nm is attributed to the direct transition from the deep valence band to the conduction band of MoS_2. Therefore our synthesis method provided a unique example of bottom-up route for production of 2H MoS_2, showing distinct band edge transitions, without any heating or calcination under inert atmosphere. The UV-vis spectrum of as-synthesized MoS_2-RGO hybrid contains additional n-π* transition band at ca 280 nm, which is shifted from 230 nm in GO due to the reduction of GO under infrared light for 6 hr (Figure 2(b)). Similar kind of absorption behaviour has been observed for the as-synthesized MoS_2 obtained from different thiocynate sources such as NaSCN, NH_4SCN, KSCN indicating the process as a generic method for few layer MoS_2 synthesis (Figure S5, ESI).

Chemical composition and oxidation states of the synthesized MoS_2 have been studied using X-ray photoelectron spectroscopy (XPS) equipped with an Al-Kα source. Figure 2 (c) and (d) display the characteristic peaks at 232.8 eV and 229.6 eV due to the binding energy of Mo $3d_{3/2}$ and Mo $3d_{5/2}$ electrons, respectively. XPS peaks at 226.7 eV, 162.4 eV and 163.5eV are attributed to the binding energy of S 2s, S $2p_{3/2}$ and S $2p_{1/2}$ electrons, respectively. By measuring the area under the curves of Mo 3d and S 2p peaks and taking account of atomic sensitivity factors, the estimated atomic ratio of Mo to S is found to be nearly stoichiometric ~1:2.04 in as-synthesized MoS_2. The formation of MoS_2-RGO hybrid and extent of reduction of graphene oxide can be estimated by comparing oxygenated carbon present in narrow scan region of C 1s in the XPS analysis (Figure S6, ESI)

Atomic force microscopy (AFM) has been used for the characterization of 2D materials for precise mapping of the thickness, morphology and lateral dimension of layered structure. The AFM image in Figure 3 (a) reveals a flat MoS_2 flake with a typical lateral size of ca. 1.0 µm. The height profile shown in Figure 3 (b) measures the thickness of that flake is ~ 1.5 nm indicating the formation of bi-layer MoS_2 flakes. This is an example of the formation of 2H phase MoS_2 nanosheets, synthesized without using any template by bottom up approach, which always have a tendency to produce bulk in the absence of template or stabilizer.

Raman spectroscopy, a powerful non-destructive characterization tool, enumerates very useful information for 2D materials like graphene and MoS_2. Two Raman modes, arising from in-plane vibration E^1_{2g} and out-of-plane A_{1g} are sensitive towards the thickness of MoS_2 layer.[42] Raman spectrum of thin as-synthesized MoS_2 (Figure 3(c)) exhibits two prominent peaks at 407 cm^{-1} and 383 cm^{-1} for A^1_g and E^1_{2g}, modes respectively, indicating the formation of highly pure 2H MoS_2. In comparison to bulk MoS_2, both A^1_g (405 cm^{-1}) and E^1_{2g} (380 cm^{-1}) vibrational modes are blue shifted (3 cm^{-1}) because of the edge effect of as synthesized MoS_2.[43] The characteristic separation between two Raman modes has been found to be 24 cm^{-1} in contrast to 19 cm^{-1} and 26 cm^{-1} obtained for monolayer flakes and bulk MoS_2, respectively, suggesting that the synthesized MoS_2 are few layers.[44]

Further investigations have been carried out to establish the structure and crystallinity of the synthesized MoS_2 using transmission electron microscopy (TEM). Typical TEM image of the MoS_2 flakes is shown in Figure 4 (a). Transparency and lateral dimensions (200 nm to 1.2 micron) of nanosheets under electron beam confirm that hydrothermally synthesized MoS_2 sheets are very thin, which is corroborated by AFM results. Clear lattice fringes with a separation of 0.27 nm are observed for (100) planes of 2H MoS_2 in Figure 4 (b). The inset at the top right corner of Figure 4 (b) shows hexagonal arrangement of 2H MoS_2. The selected area electron diffraction (SAED) pattern of MoS_2 nanosheets in the Figure 4 (c) reveals highly crystalline nature of the sheets with hexagonal diffraction pattern.

All the sharp, intense X-ray diffraction peaks of as-synthesized layered MoS_2 and MoS_2-RGO hybrids can be identified using JCPDS file nos 37-1492 as reference for 2H MoS_2. A strong (002) peak observed (Figure 4 (d)) at 2θ of 14.1° is the characteristic feature of highly crystalline hexagonal 2H-MoS_2 nanosheets. Interestingly, an additional peak at a lower diffraction angle for as-synthesized MoS_2 is observed, indicating the expansion of the unit cell due to in-situ intercalation cations, primarily along the c axis.[45] Compared with the diffraction pattern of pristine bulk MoS_2, the other featured peaks for (103), (105) planes of MoS_2 are absent, indicating the formation of very thin layer of MoS_2. The presence of ions or gases at a high pressure inside the autoclave prevents the growth of MoS_2 in the vertical directions. To get an insight about the layer formation of MoS_2, we have changed the counter cation of thiocyante anion with K or Na. Surprisingly, we found that the peak for 2θ at 8.08° changes to 9°, indicating the incorporation of K^+ ion for K-MoS_2 and hydrated sodium ion for Na-MoS_2, and NH_4-MoS_2. XRD has also been used to characterize MoS_2-GO and MoS_2-RGO hybrids. An additional sharp peak in the MoS_2-GO composite at 12.67° and a broad peak at 22.5° are assigned as the (002) peak of GO nanoflakes (Figure S7, ESI). We can hardly detect the (002) peak of RGO at 2θ around 25°, indicating that the graphene nanosheet seldom stacks together in presence of MoS_2 layer. [46] Two new diffraction peaks for (001) and (003) planes indicate that graphene or the cations (Na or K) remains in the Van der Waal gap of the MoS_2 layer.

The aforementioned results reveal that the bottom up synthesized MoS_2 exhibits high crystallinity, well resolved excitonic absorption peaks and semiconducting nature in few layer thick 2D structure. Controlling the crystal growth only in lateral direction, inhibiting along c-axis is crucial to obtain 2D MoS_2 over 3D MoS_2. For example, Park *et al.*[47] obtained 2D

MoS_2 using graphene template and acetic acid additive, which hinder the growth along c-axis. Herein, without using any template or additives, which may destroy the intrinsic nature of MoS_2, 2D MoS_2 could be obtained on attenuating the growth along lateral direction by cations and gaseous by-products present in the reaction mixture. Liu *et al.*[48] reported the growth of low crystalline few-layered MoS_2 nanosheet on stannous oxide (SnO_2) nanotube by reduction with hydrazine, a toxic and explosive chemical at hydrothermal condition. In contrast, our hydrothermal approach used thiocyanate anion as a reducing agent, avoiding hydrazine, or any other toxic chemicals. Moreover, 2D MoS_2 samples can be grown with highly crystallinity using a one pot method, by exempting thermal annealing step under inert atmosphere.

The absorption spectra of as-synthesized 2D MoS_2 in the visible region makes it attractive for the fabrication of photodiodes integrated on Si substrates similar to graphene oxide/Si heterostructure.[49] Carrier type of the synthesized MoS_2 was determined by Hall measurement in van der Pauw configuration. The measurement at room temperature revealed a negative Hall co-efficient of 0.97×10^{-4} m^3/C, which is the evidence of n-type nature. This is an agreement with the doping behavior of MoS_2 reported in the literature[21] from the transfer characteristic of fabricated transistor. The schematic diagram of the fabricated p-Si/MoS_2 heterojunction device is presented in Figure 5 (a). Typical current-voltage (I−V) characteristics of the fabricated heterojunction device are shown in Figure 5(b) under dark and illumination conditions. The asymmetric I−V nature establishes the formation of a junction diode between p-Si and n-MoS_2 layers.[49] The I-V characteristic exhibits a diode-like behavior with a rectification ratio of approximately 10^4 at a bias voltage of $\pm$ 3 V, while the leakage current is fairly higher compared to the ideal one. The relatively higher leakage current across the junction is attributed to the presence of high density interfacial defect states and a thin insulating native oxide passivation layer at the interface of Si and MoS_2. It should be noted that the deposited MoS_2 flakes on Si substrate are hydrothermally synthesized and spin coated onto Si, which may be accompanied with some chemical impurities at the surface/interface regime. The above diode characteristics can be significantly enhanced by lowering the defect density at the interface. However, the current level ($\sim10^{-5}$A) is significantly enhanced by an order of 10^3 at the -2 V applied bias upon the illumination of 514 nm. The irradiation of a light source (3mW/cm^2) onto the junction leads to the generation of the photon induced electron-hole pairs, and resultant photocurrent. Optical responsivity (R), is a very important parameter to establish the efficiency of a detector performance, which is defined as the ratio of photocurrent per unit area to the incident light density, at a particular wavelength: $R(\lambda) = J_{ph}/P_{opt}$, where J_{ph} is the photocurrent density and P_{opt} is the intensity of incident light. The spectral response of the fabricated device over a wavelength range of 400-800 nm is depicted in Figure 5 (c). The broad spectral response of MoS_2/Si junction is attributed the combination of charge carrier generation from direct, indirect and deep valence band to conduction band transitions under illumination. In the case of weak exciton binding, as for MoS_2 at room temperature, the photoresponse spectrum mimics the absorption spectrum. The absorption spectra exhibited three features, a strong broad peak at ~450 nm due to the deep valance band to conduction band edge transition at direct band gap position (K= 0 point). Accompanying two small but distinct peaks at ~ 618 nm and ~ 665 nm are contributed by the transitions from the maxima of splitted valance band to the minima of conduction band located at the same point. In addition, the effect of an indirect-gap transition is found to be around ~1.59 eV.[50] The above mentioned absorption characteristics of MoS_2 and the contribution of electric field interaction of MoS_2-Si resulted in the broad spectral range of photo detection, covering 400-800 nm.

The responsivity increases initially with applied bias due to the efficient collection of photocarriers at the electrodes and thereafter saturates at a higher bias increased furthermore.

The noticeable point is that the device has shown good response even for zero bias which is very useful for low power dissipation applications. The peak responsivity is found to be ~ 45 mA/W for -2 V applied bias. The responsivity can be further improved by the fabrication of a single nanoscale device.[51] The optical switching characteristics of the fabricated device with different incident power recorded under the illumination of 514 nm are shown in Figure 5 (d). The device exhibits a sharp ON/OFF current ratio of $\sim 10^3$ upon pulse exposure, which makes the diode attractive for an optical switch. With increase of the irradiation power, the rate of photogenerated carrier is enhanced but the responsivity shows a sub-linear dependence on the incident power density.

We also investigated the photocatalytic properties of the synthesized MoS_2 using dye degradation experiment. Four different as-synthesized samples, bare MoS_2, bare RGO, MoS_2-GO and MoS_2-RGO hybrids have been utilized to examine the photocatalytic behaviour. Figure 6 (a) displays the absorption spectra of Rhodamine-B (λ_{max} = 553 nm) collected at an interval of 25 min from the dye degradation reaction mixture under visible light for MoS_2-RGO hybrid. A large decrease in absorbance with increasing duration confirms the efficient dye degradation of synthesized MoS_2-RGO (MoS_2: RGO::9:1) hybrid under visible light irradiation. We did not find any obvious blue-shift of the absorbance peak at 553 nm (corresponding to *N*-de-ethylation) using our MoS_2-RGO hybrids unlike the observation on RhB degradation using MoS_2-BiOBr.[52] This suggests that the degradation of RhB occurs mainly via the destruction of the conjugated structure in the presence of MoS_2-RGO catalyst. To observe the individual role of MoS_2 and graphene sheets for photocatalytic behaviour, we performed a few control studies using RGO, bare MoS_2, and MoS_2-GO as photocatalysts. From the ratio of final to initial concentration (C/Co) vs. time curve (Figure 6(b)), it is evident that each component (i.e, MoS_2 or graphene (RGO)), has a crucial role in the photoctalytic process. RhB dye adsorption capacity of the each components is indicated by bar plot (Figure 6 (c)), which shows that MoS_2-RGO and MoS_2-GO hybrids have almost same adsorption capacity. But the photocatalytic behaviour under visible light is dramatically different for MoS_2-RGO from MoS_2-GO. The presence of conducting RGO in MoS_2-RGO hybrid facilitates enhanced charge separation and high degree of dye degradation as compared to MoS_2-GO. The presence of GO in MoS_2-GO possibly traps the charge and inhibits the degradation process. Interestingly, it is observed that the percentage adsorption of MoS_2-RGO (5 mg) hybrid is the sum of adsorption of bare MoS_2 (4.5 mg) and RGO (0.5 mg) separately. Due to the transparency (2.3% absorption for single layer) [53] in the visible region of solar spectrum, bare RGO does not show any photocatalytic activity (Figure 6(b)). Rather a slight increase in concentration of RhB is observed after stirring under light, possibly due to the desorption of the multilayer dye molecules into the solution. The photocatalysis process is mainly governed by three factors, which are the adsorption of pollutant dye molecules, the light absorption by photocatalyst and the charge separation and transportation.

The presence of RGO creates a charge separation interface in MoS_2-RGO hybrids and therefore the rate constant value of MoS_2-RGO ($k = 9.1\times10^{-3}\ min^{-1}$) for RhB degradation is higher in comparison to that of bare MoS_2 ($k = 4.5\times10^{-3}\ min^{-1}$). The effect of RGO content on dye degradation process is shown in the Figure S8, ESI. Upon addition of 5 % RGO in $MoS_{2,}$ the MoS_2-RGO catalyst has shown higher rate of photocatalysis compared to bare $MoS_{2,}$ whereas a complete decolorisation occurs using MoS_2-RGO (9:1) hybrid. However, with increasing amount of RGO in MoS_2 (20% RGO) the photon absorption decreases and the degradation poccess becomes slower. Therefore, a 9:1 ratio of MoS_2 and RGO in MoS_2-RGO hybrid is found to be optimum for creating good interface and high photon absorption, leading to efficient photocatalytic degradation of RhB dye. From these phenomena, we believe that MoS_2 is the main light harvesting component i.e. photocatalyst for the generation of electron hole pairs, whereas conducting RGO functions as a promoter for increasing the transport of photogenerated electrons and retarding the charge recombination.

To investigate the reactive species involved in the visible light driven degradation process, few control experiments in presence of hole scavenger (TEOA), hydroxyl radical scavenger (t-BuOH) and in absence of O_2 (under nitrogen environment) have been carried out. With the introduction of different scavengers into the RhB-photocatalyst mixture, the photodegradation efficiencies have been fund to decrease (Figure S9) and the photocatalyst becomes inactive for TEOA. Thus the 'holes' created on visible light illumination play a significant role in the photocatalytic degradation process, as shown schematically in the Figure 6 (d).

Furthermore, it has been observed that with the decrease of the oxygenated carbon (confirmed from XPS analysis in Figure S6, ESI) on reduction of MoS_2-GO hybrid, there is an increase in the degree of RhB degradation (Figure S10, ESI). The enhanced photocatalytic degradation of RhB dye by MoS_2-RGO hybrid is attributed to the following factors (i) better interactions between π- electrons of organic molecules and the aromatic regions of RGO which facilitates the adsorption of dye molecule onto photocatalysts; (ii) the stabilization of hydrophobic MoS_2 by RGO in aqueous medium; and (iii) the intimate contact interface between MoS_2 and RGO can facilitating the effective charge separation which allow the prompt migration of photo induced charge, resulting in an efficient photocatalytic reaction.

Conclusion

In this paper, we presented a novel hydrothermal synthesis method for highly crystalline few layer semiconducting 2H MoS_2 flakes, which is integrated with p-Si and RGO for their applications in photodetection and photocatalysis, respectively, under the visible light illumination. In the template-free synthesis process, thiocyanate anion plays dual role, both as a reducing agent, as well as S source resulting in gaseous by-products and cations, which inhibit the growth along c-axis. Excitonic absorption peaks at 618 nm and 665nm confirm the semiconducting nature of the bottom up synthesized few layers 2H MoS_2 flakes. Hydrothermally synthesized semiconducting MoS_2 has been integrated on p-Si to fabricate heterojunction diode that exhibited high rectification ratio (> 10^3) and a broad band photo-response over the visible region, indicating its potential for future Si CMOS compatible optical devices. Synthesized MoS_2-RGO hybrid exhibits superior photocatalytic ($k = 9.1\times10^{-3}$ min^{-1}) behaviour compared to bare MoS_2 ($k = 4.5\times10^{-3}$ min^{-1}) for the degradation of RhB in presence of visible light. The superiority of MoS_2-RGO hybrids over as-synthesized MoS_2 as photocatalysts is attributed to the high adsorption capacity and efficient charge separation resulting from intimate contact between MoS_2 and RGO.

Acknowledgements

AM acknowledges Department of Science and Technology (DST), India for the financial support (Project No: IFA 13-MS-09). SKR acknowledges Council of Scientific and Industrial Research, Govt. of India for 03(1275)/13/EMR-II project grant. The use of XPS facility supported by DST FIST project is gratefully acknowledged.

References

1. C. Zhang, Z. Wang, Z. Guo and X. W. (D.) Lou, *ACS Appl. Mater. Interfaces*, 2012, **4**, 3765−3768.
2. H. Li, K. Yu, H. Fu, B. Guo, X. Lei and Z. Zhu, *J. Phys. Chem. C*, 2015, **119**, 7959–7968.
3. K. Zhang, H.-J. Kim, X. Shi, J.-T. Lee, J.-M. Choi, M.-S. Song and J. H. Park, *Inorg. Chem.*, 2013, **52**, 9807−9812.
4. M. Shanmugam, T. Bansal, C. A. Durcan and B. Yu, *Appl. Phys. Lett.*, 2012, **100**, 153901-153904.
5. X. Gu, W. Cui, H. Li, Z. Wu, Z. Zeng, S.-T. Lee, H. Zhang and B. A. Sun, *Adv. Energy Mater.*, 2013, **3**, 1262–1268.

6. C-J. Liu, S-Y. Tai, S-W. Chou, Y-C. Yu, K.-D. Chang, S. Wang, F. S-S. Chien, J.-Y. Lin and T-W. Lin, *J. Mater. Chem.*, 2012, **22**, 21057-21064.
7. S-Y. Tai, C-J. Liu, S-W. Chou, F. S-S Chien, J-Y. Lin and T-W. Lin, *J. Mater. Chem.*, 2012, **22**, 24753-24759.
8. Z.Wang, T. Chen, W. Chen, K. Chang, L. Ma, G. Huang, D. Cohen and J. Y. Lee, *J. Mater. Chem. A*, 2013, **1**, 2202-2210.
9. W. Zhang, P. Zhang, Z. Su and G. Wei, *Nanoscale*, 2015, **7**, 18364–18378.
10. J.-S. Kim, H. W. Yoo, H. O. Choi and H.-T. Jung, *Nano Lett.*, 2014, **14,** 5941−5947.
11. J. L. Dattatray, Y.-K. Huang, B. Liu, J. Acharya, S. N. Shirodkar, J. Luo, A. Yan, D. Charles, U. V. Waghmare, V. P. Dravid and C. N. R. Rao, *ACS Nano*, 2013, **7**, 4879–4891.
12. O. L. Sanchez, D. Lembke, M. Kayci, A. Radenovic and A. Kis, *Nature Nanotech.*, 2013, **8**, 497–501.
13. S. Mukherjee, R. Maiti, A. Midya, S. Das and S. K. Ray, *ACS Photonics*, 2015, **2**, 760−768.
14. K. Roy, M. Padmanabhan, S. Goswami, T. P. Sai, G. Ramalingam, S. Raghavan and A. Ghosh, *Nature Nanotech.*, 2013, **8**, 826–830.
15. M. Kang, Y.-A. Kim, J. M. Yun, D. Khim, J. Kim, Y. Y. Noh, K-J. Baeg and D. Y. Kim, *Nanoscale*, 2014, **6**, 12315-12323.
16. Y. Li, H. Wang, L. Xie, Y. Liang, G. Hong and H. Dai, *J. Am. Chem. Soc.*, 2011, **133**, 7296–7299.
17. Y. Liu, Y.-X. Yu and W.-D. Zhang, *J. Phys. Chem. C*, 2013, **117,** 12949−12957.
18. Q. Li, N. Zhang, Y. Yang, G. Wang and D. H. L. Ng, *Langmuir*, 2014, **30**, 8965−8972.
19. J. N. Coleman, M. Lotya, A. O'Neill, S. D. Bergin, P. J. King, U. Khan, K. Young, A. Gaucher, S. De, R. J. Smith, I. V. Shvets, S. K. Arora, G. Stanton, H.-Y. Kim, K. Lee, G. T. Kim, G. S. Duesberg, T. Hallam, J. J. Boland, J. J. Wang, J. F. Donegan, J. C. Grunlan, G. Moriarty, A. Shmeliov, R. J. Nicholls, J. M. Perkins, E. M. Grieveson, K. Theuwissen, D. W. McComb, P. D. Nellist and V. Nicolosi, *Science*, 2011, **331**, 568−571.
20. K. S. Novoselov, D. Jiang, F. Schedin, T. J. Booth, V. V. Khotkevich, S. V. Morozov, and A. K. Geim, *Proc. Natl. Acad. Sci. U.S.A.*, 2005, **102**, 10451−10453.

21. B. Radisavljevic, A. Radenovic, J. Brivio, V. Giacometti and A. Kis, *Nat. Nanotech.*, 2011, **6**, 147-150.
22. D. Voiry, H. Yamaguchi, J. Li, R. Silva, D. C. B. Alves, T. Fujita, M. Chen, T. Asefa, V. B. Shenoy, G. Eda and M. Chhowalla, *Nat. Mater.,* 2013, **12**, 850-855.
23. J. Zheng, H. Zhang, S. Dong, Y. Liu, N. C. Tai, S. H. Suk, H. Y. Jeong, B. Liu and K. P. Loh, *Nature Commun.*, 2014, **5**, 2995.
24. P. Joensen, R. F. Frindt and S. R. Morrison, *Mater. Res. Bulletin,* 1986, **21**, 457–461.
25. G. Eda, H. Yamaguchi, D. Voiry, T. Fujita, M. Chen and M. Chhowalla, *Nano Lett.*, 2011, **11**, 5111-5116.
26. S. S Chou, Y-K. Huang, J. Kim, B. Kaehr, B. M. Foley, P. Lu, C. Dykstra, P. E. Hopkins, C. J. Brinker, J. Huang and V. P. Dravid, *J. Am. Chem. Soc.*, 2015, **137**, 1742−1745.
27. Z. Tang, Q. Wei and B. Guo, *Chem. Commun.*, 2014, **50**, 3934-3937.
28. W. Gao, M.; Wang, C. Ran and L. Li, *Chem. Commun.*, 2015, **51**, 1709-1712.
29. Y.-H. Lee, X.-Q. Zhang, W. Zhang, M. -T. Chang, C.-T Lin, K.-D. Chang, Y.-C. Yu, J. T.-W. Wang, C.-S. Chang, L.-J. Li and T.-W. Lin, *Adv. Mater.*, 2012, **24**, 2320-2325.
30. S. Wang, K. Li, Y. Chen, H. Chen, M. Ma, J. Feng, Q. Zhao and J. Shi, *Biomaterials*, 2015, **39**, 206-217.
31. K. Chang and W. Chen, *ACS Nano*, 2011, **5**, 4720-4728.
32. H. Li, L. Ma, W-x. Chen and J-m. Wang, *Materials Letters*, 2009, **63**, 1363–1365.
33. P. Afanasiev, L. Rawas and M. Vrinat, *Mater. Chem. Phys.*, 2002, **73**, 295–300.
34. C. Altavilla, M. Sarno and P. Ciambelli, *Chem. Mater*., 2011, **23**, 3879–3885.
35. A. Midya, V. Mamidala, J. X. Yang, P. K. L. Ang, Z.-K. Chen, W. Ji and K. P. Loh, *Small*, 2010, **6**, 2292-2300.
36. Y. Peng, Z. Meng, C. Zhong, J. Lu, W. Yu, Z. Yang and Y. Qian, *J. Solid State Chem.* 2001, **159**, 170-173.
37. G. S. Bang, K. W. Nam, J. Y. Kim, J. Shin, J. W. Choi and S-Y. Choi, *ACS Appl. Mater. Interfaces*, 2014, **6**, 7084−7089.
38. N. Wang, F. Wei, Y. Qi, H. Li, X. Lu, G. Zhao and Q. Xu, *ACS Appl. Mater. Interfaces*, 2014, **6**, 19888–19894.
39. R. Maiti, A. Midya, C. Narayana and S. K. Ray, *Nanotechnology*, 2014, **25**, 495704.
40. D. Xiao, G.-B. Liu, W. Feng, X. Xu and W. Yao *Phys. Rev. Lett*. 2012 108.196802

41. Z. Y. Zhu, Y. C. Cheng, and U. Schwingenschlogl *Physical Review B* 2011, **84**, 153402
42. C. Lee, H. Yan, L. E. Brus, T. F. Heinz, J. Hone and S. Ryu, *ACS Nano*, 2010, **4**, 2695–2700.
43. S. Mathew, K. Gopinadhan, T. K. Chan, X. J. Yu, D. Zhan, L. Cao, A. Rusydi, M. B. H. Breese, S. Dhar, Z. X. Shen, T. Venkatesan and J. T. L. Thong, *Appl. Phys. Lett*., 2012, **101**, 102103.
44. X. Yu, M. S. Prevot and K. Sivula, *Chem. Mater.*, 2014, **26**, 5892–5899.
45. A. Zak, Y. Feldman, V. Lyakhovitskaya, G. Leitus, R. Popovitz-Biro, E. Wachte, H. Cohen, S. Reich and R. Tenne, *J. Am. Chem. Soc*., 2002, **124**, 4747-4758.
46. Y. Liu, Y. Zhao, L. Jiao, and J. A. Chen, *J. Mater. Chem. A*, 2014, **2**, 13109-13115.
47. K. Zhang, H.-J. Kim, X. Shi, J. T. Lee, J. M. Choi, M. S. Song and J. H. Park, *Inorg. Chem*. 2013, **52**, 9807−9812.
48. Y. Huang, Y.-E. Miao, L. Zhang, W. W. Tjiu, J. Pan and T. Liu, *Nanoscale*, 2014, **6**, 10673-10679.
49. R. Maiti, S. Manna, A. Midya and S. K. Ray, *Opt. Express*, 2013, **21**, 26034-26043.
50. K. F. Mak, C. Lee, J. Hone, J. Shan and T. F. Heinz, *Phys. Rev. Lett.*, 2010, **105**, 136805
51. K. Das, S. Mukherjee, S. Manna, S. K. Ray and A. K. Raychaudhuri, *Nanoscale*, 2014, **6**, 11232.
52. J. Di, J. Xia, Y. Ge, L. Xu, H. Xu, J. Chen, M. He and H. Li, *Dalton Trans.*, 2014, **43**, 15429-15438.
53. R. R. Nair, P. Blake, A. N. Grigorenko, K. S. Novoselov, T. J. Booth, T. Stauber, N. M. R. Peres and A. K Geim, *Science*, 2008, **320**, 1308.

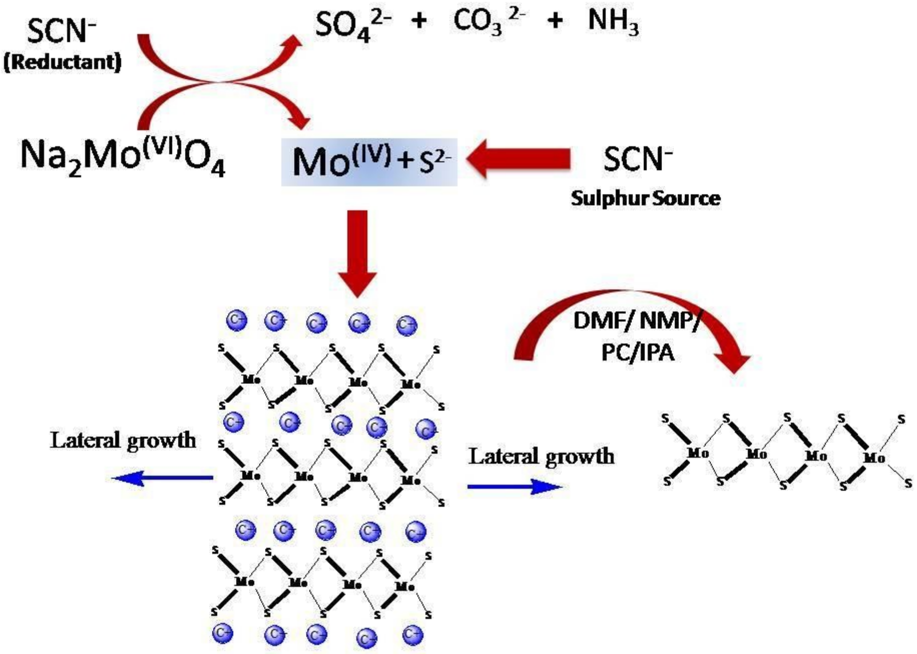

Figure 1. Synthesis scheme of 2H MoS_2 layers; cations present in the reaction mixture hinder vertical growth, allowing lateral growth in two dimension.

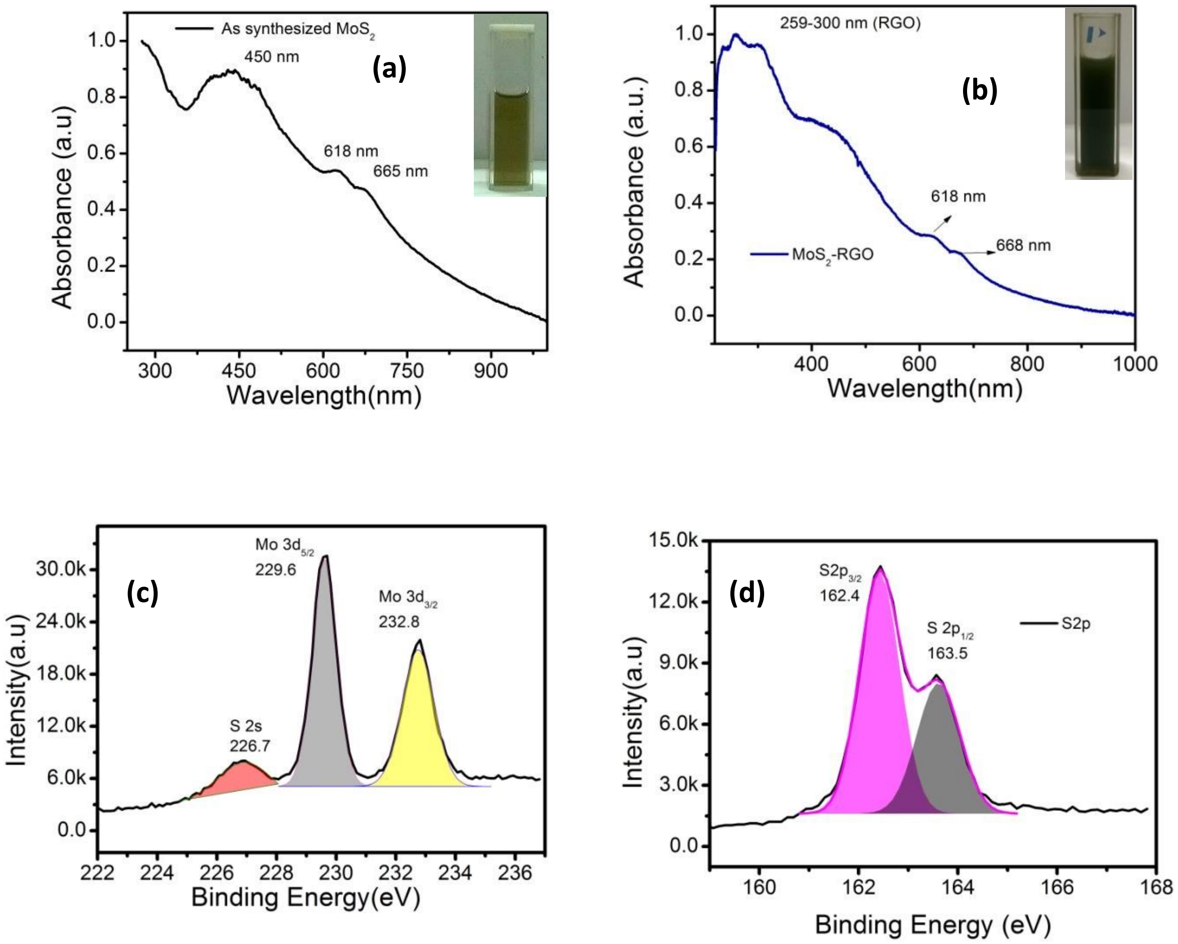

Figure 2. Typical UV-visible absorption spectra of (a) solution processed MoS_2 using IPA solution and digital image of MoS_2 in IPA (inset); (b) MoS_2-RGO (6 hr reduction) showing photothermal stability and digital image of MoS_2-RGO in water. (inset); High resolution XPS spectra showing the binding energy of (c) Mo 3d, S 2s and (d) S 2p electrons

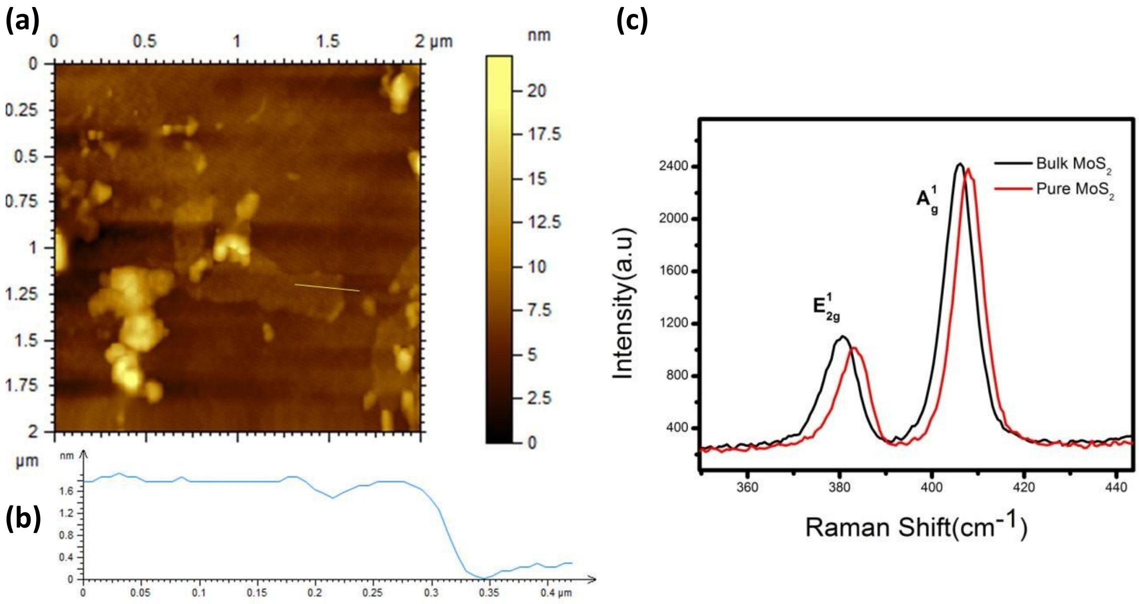

Figure 3. (a) Typical AFM image of as-synthesized MoS$_2$ layer; and (b) height profile of the 2H-MoS$_2$; (c) Raman spectra of as-synthesized MoS$_2$ flakes showing in-plane and out-of-plane vibrational mode. The spectrum of bulk MoS$_2$ is shown for comparison

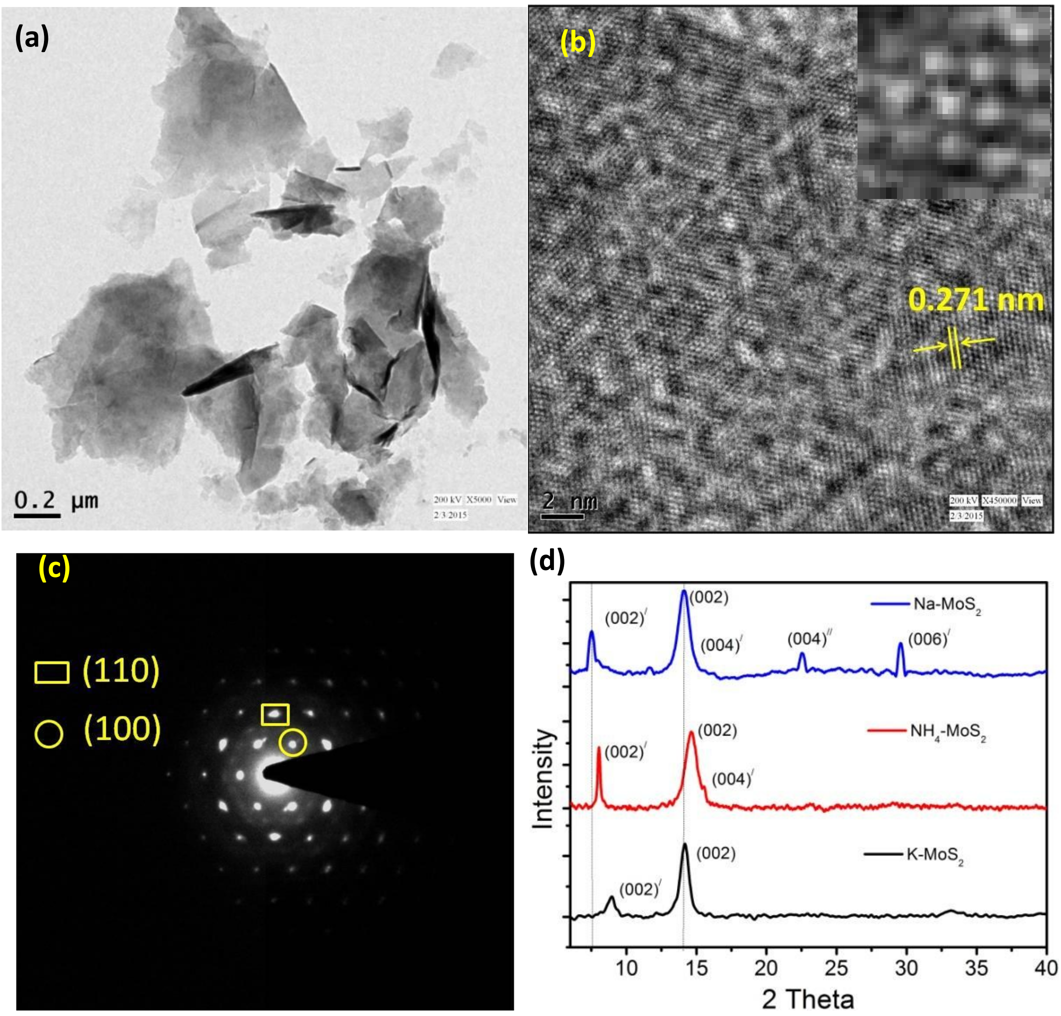

Figure 4. (a) Typical TEM image of as-synthesized MoS_2 showing micron sized flakes; (b) HRTEM image of MoS_2 showing lattice fringes and hexagonal arrangement of atoms(in the inset); (c) SAED pattern of as-synthesized MoS_2 indicating highly crystalline structure. XRD pattern of as synthesized MoS_2 using NaSCN, NH_4SCN and KSCN are depicted as Na-MoS_2, NH_4-MoS_2 and K-MoS_2, respectively.

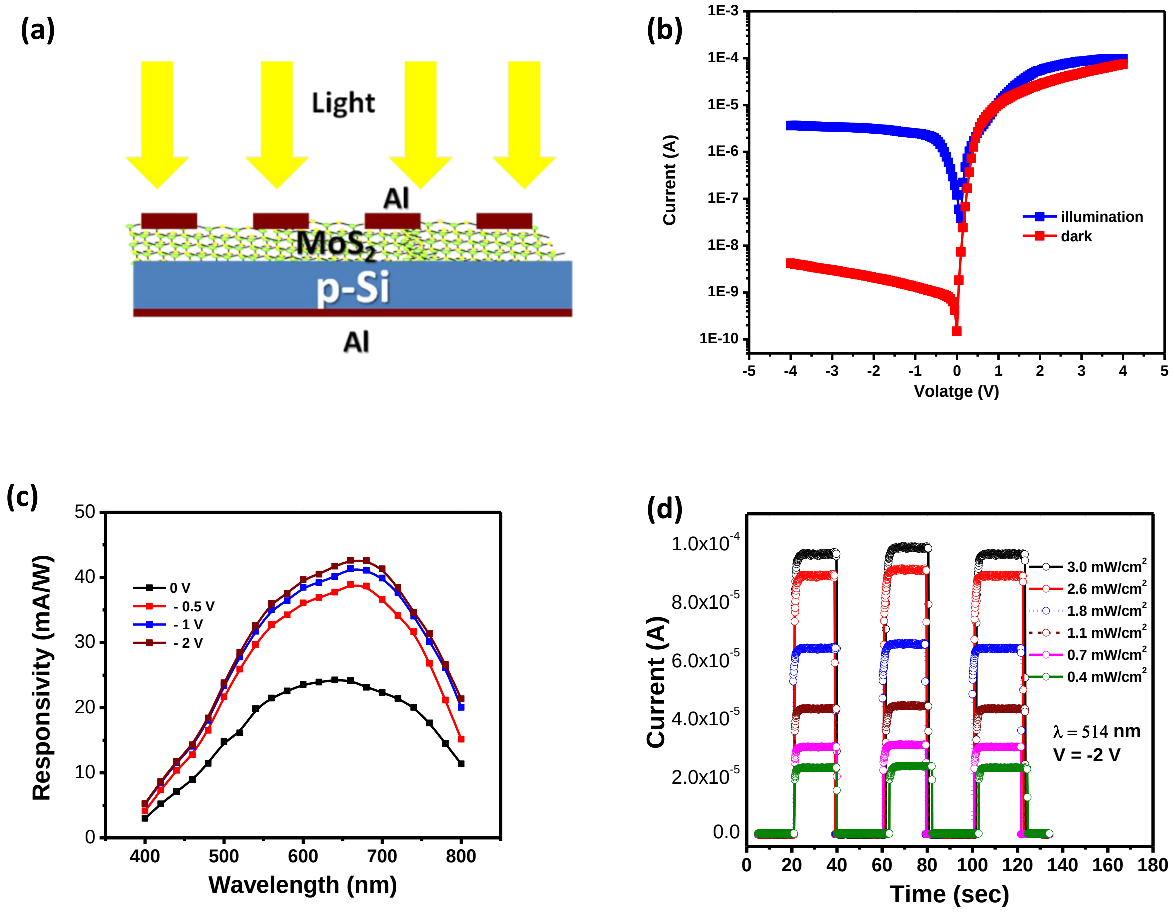

Figure 5. (a) Schematic cross-sectional view of the fabricated heterojunction device; (b) typical current-voltage characteristics of the fabricated p-n diode under dark and illuminated condition; (c) Spectral selectivity of the device with a peak response of ~ 45 mA/W over the visible region; (d) Optical switching characteristics of the devices upon illumination of different power density

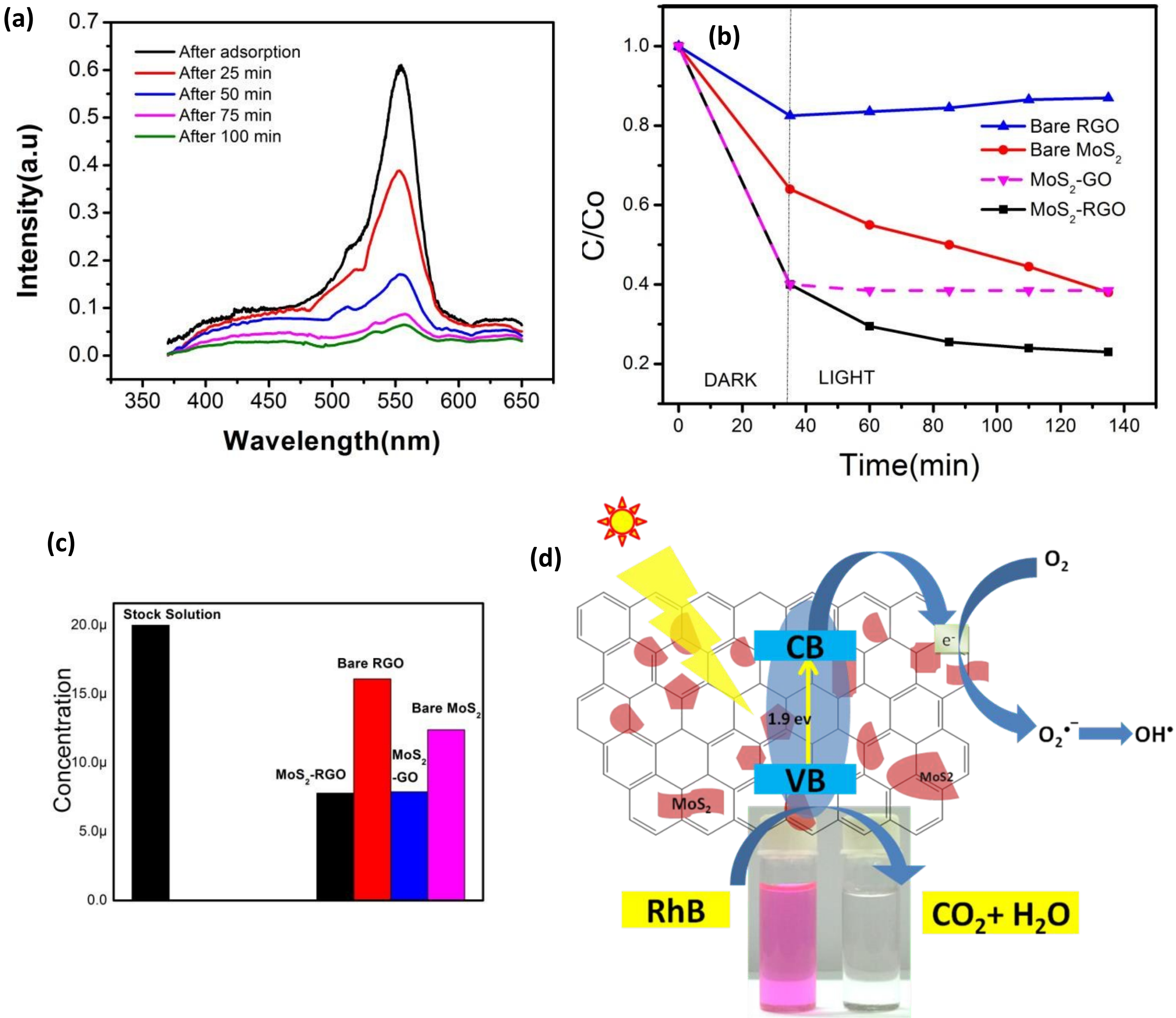

Figure 6. (a) Evolution of UV-vis absorption spectra as a function of time during the photocatalytic degradation of RhB in aqueous solution in the presence of MoS_2- RGO hybrid; b) C/Co vs time plot for three different catalyst compositions; (c) Bar plot showing concetration of RhB remaining in the solution after 35 min; (d) schematic diagram of photocatalytic RhB degradation using MoS_2-RGO hybrid.

TOC:

Template Free Bottom-up Synthesized Micron Sized Few Layer 2H MoS_2 For Photodetector and photocatalytic applications